Enhanced thermoelectric performance of solution-derived bismuth telluride based nanocomposites via liquid-phase Sintering

Chaohua Zhang[1], Maria de la Mata[2], Zhong Li[3], Francisco J. Belarre[2], Jordi Arbiol[2,4], Khiam Aik Khor[3], Dario Poletti[5], and Qihua Xiong[1,*]

[1]*Division of Physics and Applied Physics, School of Physical and Mathematical Science, Nanyang Technological University, 637371 (Singapore)*

[2]*Catalan Institute of Nanoscience and Nanotechnology (ICN2), CSIC and the Barcelona Institute of Science and Technology, Campus UAB, Bellaterra, Barcelona, 08193 (Spain)*

[3]*School of Mechanical and Aerospace Engineering, Nanyang Technological University, 639798 (Singapore)*

[4]*Institució Catalana de Recerca i Estudis Avançats (ICREA), Barcelona, 08010 (Spain)*

[5]*Singapore University of Technology and Design, 8 Somapah Road, 487372 (Singapore)*

*To whom correspondence should be addressed. E-mail: qihua@ntu.edu.sg

Abstract

Bismuth telluride based thermoelectric materials show great promise in electricity generation from waste heat and solid-state refrigeration, but improving their conversion efficiency with economical approaches for widespread use remains a challenge. We have developed a scalable bottom-up solution-chemistry approach to obtain nanostructured powders, which are used to build bulk thermoelectric materials by the spark plasma sintering process. Using excess tellurium as sacrificial additive to enable liquid-phase-sintering, the lattice and bipolar contributions to the thermal conductivity are both greatly reduced, which leads to the achievement of high figure of merit (ZT) in _both_ n-type and p-type bismuth telluride based nanocomposites. The ZT values are 1.59±0.16 for p-type $Bi_{0.5}Sb_{1.5}Te_3$ and 0.98±0.07 for n-type $Bi_2Te_{2.7}Se_{0.3}$ at 370 K, which are significantly high for bottom-up approaches. Our results demonstrate that solution-chemistry approaches as facile, scalable and low-energy-intensive ways to achieve nanopowders, can open up great possibilities in developing high-performance low-price bulk nanocomposites for commercial thermoelectric applications.

Power generation by converting waste heat into useful electricity and cryogen-free solid-state refrigeration are the two major applications for thermoelectric materials[1], which are significant for combating the energy and global warming challenges. Improving the conversion efficiency of thermoelectric materials and developing economical materials and preparing methods are crucial for the widespread use of thermoelectric products[2]. The efficiency of thermoelectric materials is determined by the materials' dimensionless figure of merit (ZT), where $ZT=(S^2/\rho\kappa)T=(PF/\kappa)T$, and S, ρ, κ, T, PF are the Seebeck coefficient, electrical resistivity, thermal conductivity, absolute temperature, and power factor, respectively. Nanostructuring process has been widely proposed to enhance the ZT value of

thermoelectric materials by reducing the thermal conductivity without significantly depressing the power factor[3-10]. Generally, nanostructuring processes to bulk thermoelectric materials can be divided into two steps: producing nanostructured powders and sintering powders to bulk composite materials. Top-down approaches using bulk ingots as starting materials like ball-milling[6,11] and melt-spinning[9,12] are widely used to obtain nanostructured powders for ZT-improved bulk materials, but these methods are usually energy-intensive. Bottom-up approaches from chemical precursors like chemical solution synthesis are facile, scalable and low-energy-intensive ways to achieve nanostructured powders[13], which thus exhibit considerable promise for fabricating commercial thermoelectric devices at low cost if their ZT values can be further improving by improving the power factor.

Among the big family of thermoelectric materials in all temperature ranges, bismuth telluride (Bi_2Te_3)-based materials (like p-type $Bi_xSb_{2-x}Te_3$ and n-type $Bi_2Te_{3-y}Se_y$) are the most widely-used thermoelectric bulk materials near room temperature region[14]. Commercial Bi_2Te_3-based ingots are prepared by the solid solution alloying method[15], whose ZT peaks have remained at about 1 near room temperature for nearly 50 years. There have been consecutive efforts to improve their ZT values by nanostructuring process since the start of this century[6,7,9,10,12,16-19]. For p-type $Bi_xSb_{2-x}Te_3$, ZT peaks >1.4 around 370-390 K have been achieved using the ball-milling[6] and melt-spinning process[12]. Recently, a higher ZT peak value ~1.86 near 320 K for p-type bulk $Bi_{0.5}Sb_{1.5}Te_3$ has been achieved by a modified melt-spinning process with excess tellurium as sacrificial additive[9]. The ZT improvement of n-type bulk $Bi_2Te_{3-y}Se_y$ is still limited, whose highest recorded ZT value is still around 1.1 to 1.2 in the range 350-400 K by ball-milling[19] and hot-deformation process[20]. Various bottom-up solution synthesis methods have also been reported to scale up these nanostructured Bi_2Te_3-based materials[7,18,21-35], but resultant composites usually show much lower ZT values compared with the ones made by top-down methods. The achieved ZT value of both n-type

and p-type Bi_2Te_3-based materials varies much between different bottom-up chemistry approaches, which can be ranged from 0.04[35] to 1.1[7], and most of them are lower than 1 in the temperature range 300-400 K[18,21-34]. The high electrical resistivity and low power factor are the main obstacles for achieving high ZT in those solution-synthesis samples even though their thermal conductivity can be greatly reduced[13]. Reducing the thermal conductivity without compromising much of the power factor remains a challenge for bottom-up chemistry approaches.

In this study we report that high-thermoelectric performance of p-type $Bi_{0.5}Sb_{1.5}Te_3$ and n-type $Bi_2Te_{2.7}Se_{0.3}$ nanobulk materials can be realized by the bottom-up solution-synthesis and spark plasma sintering (SPS) approach, by introducing excess tellurium during chemical synthesis. This excess tellurium works as a sacrificial additive to enable liquid-phase-sintering, which is effectively for reducing the thermal conductivity without compromising the power factor much. ZT values as high as 1.59±0.16 for p-type $Bi_{0.5}Sb_{1.5}Te_3$ and 0.98±0.07 for n-type $Bi_2Te_{2.7}Se_{0.3}$ are obtained at 370 K, much higher than other reports using chemical approaches, opening up great possibilities for the commercial use of chemically scalable bulk nanocomposites in solid-state refrigeration and low-temperature power generation.

Results and discussions

Bottom-up approach for nanostructured bulk thermoelectric materials. Based on our previous experiments on the wet-chemical synthesis of pnictogen chalcogenide nanocrystals like Bi_2Se_3[36], p-type $Bi_xSb_{2-x}Te_3$ [28] and n-type $Bi_2Te_{3-y}Se_y$[25,26], we introduced excess tellurium in the synthesis process for preparing Te-$Bi_2Te_{2.7}Se_{0.3}$ and Te-$Bi_{0.5}Sb_{1.5}Te_3$ mixtures. In this modified solution synthesis method, Bi, Sb, Te, Se related precursors mixing with other supporting chemical compounds were dissolved in ethylene glycol or diethylene glycol solvent for reaction at the boiling temperatures of the solvents. As displayed in Figure 1a, the

facile solution synthesis is carried out in a flask heated by electrothermal mantel for about 3 hours, producing black precipitates in the solution. Powders are collected from the precipitates, and are finally produced into bulk pellets by SPS process (Figure 1a). The precipitates consist of nanoplates and nanowires as shown in the scanning electron microscopy (SEM) images of solution-grown Te-$Bi_2Te_{2.7}Se_{0.3}$ and Te-$Bi_{0.5}Sb_{1.5}Te_3$ mixtures (Figure 1b and 1c). Solution-grown Te nanocrystals in our growth conditions usually reveal the nanowire or nanocrystal morphology, while $Bi_2Te_{2.7}Se_{0.3}$ and $Bi_{0.5}Sb_{1.5}Te_3$ are nanoplate-shapes[26,28]. The X-ray diffraction (XRD) spectra of those collected powders also reveal that solution-derived Te-$Bi_2Te_{2.7}Se_{0.3}$ and Te-$Bi_{0.5}Sb_{1.5}Te_3$ are the mixtures of Te and $Bi_2Te_{2.7}Se_{0.3}$, and $Bi_{0.5}Sb_{1.5}Te_3$ respectively (Figure 1d and 1e). During the SPS process at temperature 460 $^{\circ}$C (above the melting temperature of Te, which is ~450 $^{\circ}$C) and pressure 60 MPa, the excess Te are liquefied and can be expelled out from the graphite die together with other eutectic mixtures (Supplementary Fig.1). As shown in Figure 1d and 1e, no Te-related peaks can be clearly identified from the XRD spectra of the final SPS derived bulk pellets, though tiny remaining Te phase in the n-type pellets can be found by the transmission electron microscopy (TEM) characterization as shown below. Compared with powder mixture samples, the SPS derived pellets have much sharper peaks and enhanced peaks of (006), (0015) and (0018), demonstrating that those nanoplates have reorientation trends into the disc plane that perpendicular to the SPS press direction, which is also observed in our previous reports[25,26,28].

Thermoelectric transport properties. We compare the maximum ZT value of our n-type $Bi_2Te_{2.7}Se_{0.3}$ nanobulk (n-Nano) and p-type $Bi_{0.5}Sb_{1.5}Te_3$ nanobulk (p-Nano) with that of the state-of-the-art of commercial Bi_2Te_3-based n-type $Bi_2Te_{2.7}Se_{0.3}$ ingot (n-Ingot) and p-type $Bi_{0.5}Sb_{1.5}Te_3$ ingot (p-Ingot) in the temperature region 5-370 K, as shown in Figure 1f. Our thermoelectric characterizations on the n-Ingot and p-Ingot samples show that the maximum

ZT values of those ingots are ~1.0 at around 325 K to 350 K, in agreement with other reports on commercial ingots[6,9,20]. By statistically analyzing the thermoelectric measurement data of our nanobulk samples (shown in Figure 2 and Supplementary Fig. 2 and 3 for n- and p-type samples, respectively), the average maximum ZT values are calculated to be as high as 0.98±0.07 (ZT ranging from 0.93 to 1.1) for n-Nano at 370 K and 1.59±0.16 (ZT ranging from 1.35 to 1.80) for p-Nano at 370 K, which are about 2 times and 3 times higher respectively than that of our previous samples without adding excess Te in the chemical solution-growth process[26,28]. Our p-Nano samples have ~60% increase in ZT comparing with p-Ingot sample, while our n-Nano samples are comparable with the n-Ingot sample. Generally speaking, Bi_2Te_3-based commercial ingots always suffer from the crack problem along their cleavage plane, which is a disadvantage for device fabrication and integration. Introducing polycrystalline structures with smaller grains is a common way to improve materials' mechanical performance. During the cutting process of bulk materials, we did find that the annoying crack problem is quite common in commercial ingots (Supplementary Fig.4) but not happened in our nanobulk samples. Considering the enhanced thermoelectric and mechanical performance, the advantage of low-energy-intensive and facile fabrication, our bottom-up approach exhibits considerable promise towards practical applications.

Figure 2 demonstrates the temperature dependence of thermoelectric performance of the commercial ingots and our nanobulk samples in the temperature region 5-370 K, and the presented nanobulk samples are the typical samples with ZT value close to the average level of all the measured samples. All the measurements were taken in the physical properties measurement system (PPMS, Quantum Design) with the thermal transport option, using the timed single mode. The electrical resistivity of all the samples increases with temperature, which reveals their metallic behavior (Figure 2a). The electrical resistivity of our n-Nano and p-Nano is higher than that of n-Ingot and p-Ingot respectively, which can be ascribed to more

scattering introduced by nanostructures in the nanobulk samples. The Seebeck coefficient of p-Nano is close to that of p-Ingot at low and high temperatures while the Seebeck coefficient of n-Nano is slightly lower than that of n-Ingot one (Figure 2b). As shown in Figure 2c and its inset, the thermal conductivity of our n-Nano and p-Nano samples are significantly lower than that of commercial n-Ingot and p-Ingot, especially at the lower temperature (<50 K). Most importantly, as the temperature increases from 325 to 370 K, the thermal conductivity of n-Ingot and p-Ingot starts to increase while that of n-Nano and p-Nano still decreases (Figure 2c), leading to enhanced ZT values for the nanobulk samples at the high temperature region (Figure 2d). As shown in Figure 2d, the ZT of our p-Nano sample is close to that of p-Ingot below 275 K, but higher than that of p-Ingot from 300 to 370 K. On the other hand, the ZT of our n-Nano sample is slightly lower than that of n-Ingot below 350K, but it starts to prevail that of n-Ingot at 370 K (Figure 2d).

Transmission electron microscopy characterizations. To understand the mechanism of low thermal conductivity in the n-Nano and p-Nano samples, their microstructures were carefully studied by TEM (Figure 3 and Figure 4) and SEM (Supplementary Fig.5). TEM was taken on both cross-section and planar view of the SPS derived pellets that are parallel and perpendicular to the SPS press direction, respectively. Nanosized grains with different orientations are the most common features in both n-Nano and p-Nano samples (Figure 3a-d and 4a-d). Every colorr used in figures 3a-b and 4b is illustrating a different grain orientation (phase filtered HRTEM images). These nanograins are highly crystalline and have clean interfaces between boundaries, as shown in Figure 3a-d and Figure 4a-c. As shown in Figure 3g, 3i and Figure 4c-d, the typical high resolution TEM (HRTEM) images and the corresponding fast Fourier transform (FFT) indexed power spectra of n-Nano and p-Nano agree well with the cell parameters of $Bi_2Te_{2.7}Se_{0.3}$ and $Bi_{0.5}Sb_{1.5}Te_3$, respectively. For n-Nano samples, most of the regions are composed of the $Bi_2Te_{2.7}Se_{0.3}$ phase, as revealed by

energy dispersive X-ray spectroscopy (EDX) data (Supplementary Fig.6). In addition, separated Te phases are sporadically observed between boundaries, like the regions shown in Figure 3e-f. As the HRTEM image shown in Figure 3g-h, sporadic Te phase exists in the boundaries between different grains. However, we did not find segregated Te phase in the p-Nano samples, and found that most of the regions are the intended $Bi_{0.5}Sb_{1.5}Te_3$ phase (Supplementary Fig. 7). For p-Nano samples, segregation phenomenon of constituents is observed by elemental mapping of the extracted Sb and Te constituents using electron energy loss spectroscopy (EELS), as shown in Figure 4e-h. Because the characteristic EELS of Sb and Te involves overlapping between each other in some energy region, the extracted main components of the Sb and Te spectra may have deviation from pure elements (Supplementary Fig. 8), but they are related to actual features of the composition distribution in the compound. We noted that extracted Te signal mainly follows the shape of the crystals, while the extracted Sb signal is segregated to certain area, mostly in grain boundaries, as highlighted in the stacked mapping image in Figure 4h. The interface and grain boundaries in our nanobulk are drastically different than the melt-spinning composite using liquid phase sintering, in which dense dislocations are the dominant defects attributed responsible for lattice thermal conductivity reduction[9].

Reduction of the lattice thermal conductivity. Reducing the thermal conductivity κ is a big advantage of nanostructuring process for improving ZT values. Usually, the electronic thermal conductivity κ_e and lattice thermal conductivity κ_l are the two core contributions to the total thermal conductivity, though the bipolar contribution (κ_B) to the thermal conductivity by thermally generated electron and hole pairs becomes visible at high temperature regions. We determined the κ_l by subtracting κ_e from the total thermal conductivity (ignoring the bipolar contribution firstly), as displayed in Figure 5a. The κ_e was estimated according to the Wiedemann-Franz law $\kappa_e = LT/\rho$, where the Lorenz number L

was calculated using an approximation equation L=1.5+exp (-|S|/116) (where L is in the unit 10^{-8} WΩK^{-2} and S in μVK^{-1})[37], as demonstrated in Supplementary Fig. 9. The values of L at 300 K were calculated to be 1.68×10^{-8}, 1.66×10^{-8}, 1.72×10^{-8}, 1.67×10^{-8} WΩK^{-2} for p-Nano, p-Ingot, n-Nano, n-Ingot respectively. The reduction of κ_l is noticeable for our n-Nano and p-Nano samples compared to the commercial ingots, especially at the low temperature region (Figure 5a). In the low temperature region (<50 K), the large reduction of κ_l in nanobulk samples comparing with commercial ingots can be ascribed to the size effects when the mean-free path of phonons are limited by the external boundaries and imperfections[38]. At room temperature 300 K, the κ_l of p-Nano (0.38 Wm^{-1}K^{-1}) is about 2 times smaller than the p-Ingot one (0.78 Wm^{-1}K^{-1}), and the κ_l of n-Nano (0.48 Wm^{-1}K^{-1}) is also much smaller than the n-Ingot one (0.81 Wm^{-1}K^{-1}). Generally, κ_l can be expressed as a sum of contributions from different frequencies (ω)[9,38]:

$$\kappa_l = \int \kappa_s(\omega)d\omega = \int \frac{1}{3}C_p(\omega)v(\omega)l(\omega)d\omega$$

where $\kappa_s(\omega)$, $C_p(\omega)$, $v(\omega)$, $l(\omega)$ are the spectral lattice thermal conductivity, spectral heat capacity of phonons, phonon-group velocity, phonon mean-free path respectively. The $l(\omega)$ depends mainly on phonon scattering from phonon-phonon interaction (especially *Umklapp* process) and various imperfections in lattice. As different imperfections (point defects, boundaries, dislocations, nanoprecipitates) contribute to different frequency-dependent phonon scattering, a full spectrum phonon scattering strategy can be used to reduce the κ_l sufficiently[8,9]. Comparing with commercial ingots with large-size grains, our nanobulk samples have plenty of nanosized grains and boundaries as observed in TEM (Figures 3 and 4) and mesoscale grains and boundaries observed in SEM (Supplementary Fig.5). In addition, other lattice defects like segregated phase between boundaries (Te-phase in n-Nano, Sb-enrich region in p-Nano), strain, dislocations and impurity point-defects can also contribute to

different frequency phonon scattering. Thus, comparing with commercial ingots, the extra reduction of κ_l in our nanobulk samples are ascribed to these wide-frequency phonon scattering from different kinds of lattice imperfections.

Suppression of bipolar thermal conductivity. At high temperature region ($T > \theta$, θ as Debye temperature), the phonon scattering by *Umklapp* mechanism leads to a T^{-1} temperature dependence of thermal conductivity, while bipolar effect contributes to the increase of thermal conductivity at higher temperature. As shown in Supplementary Fig.10 (the graph of ($\kappa - \kappa_e$) vs 1000/T), the $\kappa - \kappa_e$ of commercial ingots is a combination of *Umklapp* process (T^{-1} dependence) and bipolar effects (T^{1} dependence). For commercial ingots, the bipolar effects start to overcome the *Umklapp* process when temperature increases above 325-350 K, leading to the increase of thermal conductivity. However, our n-Nano and p-Nano samples only exhibit the linear behaviour with T^{-1} dependence (from *Umklapp* process) from 200 K to 370 K, indicating that the bipolar thermal conductivity is greatly suppressed in our nanobulk samples. The suppression of bipolar effects has also been reported in other nanostructuring processed n-type and p-type Bi_2Te_3 based thermoelectric materials[6,39], which ascribed these effects to interfacial potential barrier from charged defects on the grain boundaries. In our nanobulk samples, the existence of nanosized grain and grain boundaries, segregated Te phase in n-Nano and Sb-enrich regions in p-Nano between boundaries can all contribute to the potential barrier in those interfaces. The potential barrier shifts the onset of bipolar thermal conductivity to higher temperatures, which results in a shift of the ZT maximum to a higher temperature. With the phonon-scattering from various imperfections and suppression of bipolar effects, the κ_l values of n-Nano and p-Nano are as low as 0.37 and 0.23 $Wm^{-1}K^{-1}$ at 370 K respectively, much lower than the n- and p- Ingot values (0.79 $Wm^{-1}K^{-1}$).

Preserving the power factor. Figure 5b shows the temperature dependence of power factors (*PF*) of our nanobulk samples comparing with that of commercial ingots. The *PF* of n-Nano, p-Nano, n-Ingot, p-Ingot at 300 K (370 K) are 2.0(1.9), 2.5(2.1), 3.6(3.2), 3.8(3.0) mWm^{-1}K^{-2}, respectively. Although the *PF* of our nanobulk samples are still lower than that of the commercial ingots, they are much higher than the values reported in most of other solution-derived nanocomposites with *PF*<1.8 mWm^{-1}K^{-2} in all temperature region[21-23,25,26,28-30,33-35]. Calculated from Hall measurements, the carrier densities *n* of the ingot and nanobulk samples are in the range 1-3×10^{19} cm^{-3} and nearly independent of the temperature (Supplementary Fig. 11). Generally, the Seebeck coefficient shows strong dependence on the carrier density[2]: $S \propto n^{-2/3}$. The carrier density in p-Nano is nearly the same with p-Ingot (~1.45×10^{19} cm^{-3} at 300 K for both), which agrees well with their nearly close Seebeck coefficient. On the other hand, the carrier density of n-Nano (2.47×10^{19} cm^{-3}) is higher than that of n-Ingot (1.83×10^{19} cm^{-3}) at 300 K, which can be the reason for the reduction of the Seebeck coefficient in n-Nano. Figure 5c demonstrates the temperature dependence of the charge-carrier mobility *μ,* calculated with the formula $\mu = 1/(n\rho e)$. Compared with ingots, the decrease of *μ* in nanobulk samples is mainly due to additional electron scattering from interfacial charge potential and boundaries. The reduction of *PF* in our nanobulk samples is compensated by the reduction of *κ*, making the thermoelectric performance of n-Nano and p-Nano samples comparable and better than that of commercial n-Ingot and p-Ingot, respectively (Figure 2d).

Liquid-phase-sintering is a widely used process for engineering materials, which involves the sintering under conditions where a wetting liquid exists between solid grains[40]. In our SPS process, the excess Te is liquefied when the sintering temperature is higher than the melting temperature of Te (450 °C), enabling the liquid-phase-sintering process. Some eutectic compositions (p-type Bi$_{0.5}$Sb$_{1.5}$Te$_3$ and n-type Bi$_2$Te$_{2.7}$Se$_{0.3}$) are also liquefied together with Te. Those liquid mixtures have high mass-diffusivity, which can quickly

penetrate into those grain boundaries. The liquid mixtures behave like glues that bond together different boundaries with good electrical connection. Compared with our previous results without adding excess Te in the solution-synthesis process[26,28], nanobulk samples in this work have much higher power factor besides having much low lattice thermal conductivity (Supplementary Fig. 12). For our p-Nano samples, the excess Te can be completely expelled out during the high-pressure compacted process, similar to the observations in p-type $Bi_{0.5}Sb_{1.5}Te_3$ when adding an excess of Te in the melt-spinning process[9]. However, our n-Nano samples still have some remaining Te phase after SPS process as observed in TEM, which can be the reason for the slight increasing in carrier concentration and decreasing in Seebeck coefficient. The microstructures of remaining Te phase in n-Nano and Sb-rich regions in p-Nao between grains can be the trace left in the Te-resulted liquid-phase sintering process. Comparing our n-Nano with p-Nano, it indicates that completely expelling out the Te phase in the SPS process is more favourable for optimizing the power factor and lattice thermal conductivity. Further improvements on the n-type nanobulk samples are still needed to optimize the carrier concentration as well as charge-carrier mobility and lattice thermal conductivity.

Conclusions

In summary, we have developed a facile bottom-up approach for the nanostructuring design of n-type $Bi_2Te_{2.7}Se_{0.3}$ and p-type $Bi_{0.5}Sb_{1.5}Te_3$ bulk samples with superior thermoelectric performance using excess Te as sacrificial additive. The average maximum ZT value of our nanobulk samples at 370 K can reach up to 1.59±0.16 for p-type $Bi_{0.5}Sb_{1.5}Te_3$ and 0.98±0.07 for n-type $Bi_2Te_{2.7}Se_{0.3}$, which is higher and comparable with the corresponding p-type and n-type commercial ingots, respectively. The ZT enhancement mainly comes from the large reduction in the lattice thermal conductivity, which can be ascribed to the broad-frequency

phonon scattering from various lattice imperfections. The increase of ZT values at high temperatures also benefits from the nanostructuring process, which leads to the suppression of bipolar thermal conductivity. Sacrificed tellurium included in our process to enable liquid-phase-sintering can be the key to maintain the power factor while introduce plenty of nanostructures for the reduction of thermal conductivity. We have proved that a great ZT enhancement can be realized by this cost-effective, facile and scalable chemical bottom-up approach. Considering the facility and full of variety in the chemical synthesis of nanomaterials, there is huge potential and great prospect for bottom-up approaches to further improve the thermoelectric performance by designing new nanostructured materials.

Methods

Chemical solution synthesis

To synthesize 4 mmol Te-excess-$Bi_{0.5}Sb_{1.5}Te_3$ mixture, 15 mmol potassium tellurite monohydrate, 2 mmol bismuth acetate, 6 mmol antimony acetate, 40 mmol potassium hydroxide and 0.4 g Polyvinylpyrrolidone (PVP, average M_w~55,000) as stabilizing agent were dissolved or dispersed in the 160 ml diethylene glycol (DEG) solvent loaded in a 250-mL round bottom flask with the help of sonication. After that, 0.4 g L-cysteine was added to the mixed solution and found the colour of solution change from white to black immediately. Then the flask was transferred to an electrothermal mantel with stirring part for heating at the boiling temperature of solution (~ 240 °C). The heating power was turned off after heating the blended solution for 3 hours, then the solution was cooled down to room temperature.

To synthesize 4 mmol Te-excess-$Bi_2Te_{2.7}Se_{0.3}$ mixture, 13.9 mmol potassium tellurite monohydrate, 1.2 mmol potassium selenite, 8 mmol bismuth acetate, 40 mmol potassium hydroxide and 0.4 g PVP (average M_w~55,000) were dissolved in the 160 ml ethylene glycol

(EG) solvent. Then the mixed solution was heated at the boiling temperature of solution (~ 190 °C) for 3 hours.

After reaction, the black precipitates were washed in acetone and isopropyl alcohol with the assistance of sonication and centrifuging. The washing process was repeated for several cycles. After that, those precipitates were left in a dry cabinet at room temperature for about 1 day. Those aggregated dry precipitates were hand ground into fine powders using an agate jar and plunger.

Preparation of bulk samples

Our nanostructured n-type $Bi_2Te_{2.7}Se_{0.3}$ and p-type $Bi_{0.5}Sb_{1.5}Te_3$ bulk samples (n-Nano and p-Nano) were produced by spark plasma sintering (SPS) of those synthesized powders at 460 °C for 3 min with an applied pressure of 60 Mpa. The commercial n-type $Bi_2Te_{2.7}Se_{0.3}$ and p-type $Bi_{0.5}Sb_{1.5}Te_3$ ingots (n-Ingot and p-Ingot) as comparing materials were purchased from the company of Thermonamic Electronics (Jiangxi) Corp., Ltd.

Using the traditional Archimedes method, the density of n-Ingot and p-Ingot were measured to be 7.75 and 6.86 g/cm^3 respectively. And the densities of our SPS yielded n-Nano and p-Nano were about 83%-91%, 86%-90% of that of n-Ingot and p-Ingot respectively. After SPS, our pellet-like bulk samples (~10.5 mm in diameter and 1-2 mm in thickness) were cut to bars with length ~10 mm, width ~2.5 mm and thickness ~1 mm. The commercial ingot samples were cut into bars along the cleavage directions having the largest ZT. To make the final samples for thermoelectric measurements, all the bars were polished with sandpapers firstly, and then four-probe leads were attached to the bars by applying the silver-filled H20E-HC epoxy.

Characterizations

X-ray diffraction (XRD) patterns were performed using a Bruker D8 advance diffractometer with Cu K$_\alpha$ radiation (λ=0.15404 nm; 40 kV, 40 mA) in the locked couple mode between the X-ray gun and detector. Morphology characterizations of the samples were taken by scanning electron microscopy (SEM, JEOL 7100F). Nanobulk samples were cut for planar and cross-section view with a diamond wire precision saw and then mechanically thinned by using diamond films. The final polishing step included conventional ion milling in a GATAN PIPS. The samples were then studied by (scanning) transmission electron microscopy (S)TEM in a FEI Tecnai F20 microscope equipped with a Quantum EELS spectrometer and EDX detectors, providing both, structural and chemical analyses.

The temperature dependence of the thermoelectric performances (parameters S, σ, and κ) was measured in a physical properties measurement system (PPMS, Quantum Design) with thermal transport option, using the single timed mode. The testing period is set from 600 s to 3000 s increasing with the test temperature, which is as long as enough to make sure the steady-state measurement at each test temperature. The thermoelectric measurements of our nanobulk samples were taken along the disc-plane direction that was perpendicular to the SPS-pressing direction and that of ingot samples are along the cleavage direction. The Hall coefficient was measured in the PPMS with AC transport option.

References

1.   Bell, L. E. Cooling, heating, generating power, and recovering waste heat with thermoelectric systems. *Science* **321**, 1457-1461 (2008).

2.   Snyder, G. J. & Toberer, E. S. Complex thermoelectric materials. *Nat. Mater.* **7**, 105-114 (2008).

3.   Minnich, A. J., Dresselhaus, M. S., Ren, Z. F. & Chen, G. Bulk nanostructured thermoelectric materials: current research and future prospects. *Energy Environ. Sci.* **2**, 466-479 (2009).

4.   Vineis, C. J., Shakouri, A., Majumdar, A. & Kanatzidis, M. G. Nanostructured thermoelectrics: big efficiency gains from small features. *Adv. Mater.* **22**, 3970-3980 (2010).

5. Biswas, K. *et al.* Strained endotaxial nanostructures with high thermoelectric figure of merit. *Nat. Chem.* **3**, 160-166 (2011).

6. Poudel, B. *et al.* High-thermoelectric performance of nanostructured bismuth antimony telluride bulk alloys. *Science* **320**, 634-638 (2008).

7. Mehta, R. J. *et al.* A new class of doped nanobulk high-figure-of-merit thermoelectrics by scalable bottom-up assembly. *Nat. Mater.* **11**, 233-240 (2012).

8. Biswas, K. *et al.* High-performance bulk thermoelectrics with all-scale hierarchical architectures. *Nature* **489**, 414-418 (2012).

9. Il Kim, S. *et al.* Dense dislocation arrays embedded in grain boundaries for high-performance bulk thermoelectrics. *Science* **348**, 109-114 (2015).

10. Yan, X. *et al.* Experimental studies on anisotropic thermoelectric properties and structures of n-type $Bi_2Te_{2.7}Se_{0.3}$. *Nano Lett.* **10**, 3373-3378 (2010).

11. Wu, D. *et al.* Significantly Enhanced Thermoelectric Performance in n-type Heterogeneous BiAgSeS Composites. *Adv. Funct. Mater.* **24**, 7763-7771 (2014).

12. Xie, W. *et al.* Identifying the specific nanostructures responsible for the high thermoelectric performance of $(Bi,Sb)_2Te_3$ nanocomposites. *Nano Lett.* **10**, 3283-3289 (2010).

13. Zhao, Y., Dyck, J. S. & Burda, C. Toward high-performance nanostructured thermoelectric materials: the progress of bottom-up solution chemistry approaches. *J. Mater. Chem.* **21**, 17049-17058 (2011).

14. Sootsman, J. R., Chung, D. Y. & Kanatzidis, M. G. New and old concepts in thermoelectric materials. *Angew. Chem. Int. Ed.* **48**, 8616-8639 (2009).

15. Yim, W. M. & Rosi, F. D. Compound tellurides and their alloys for peltier cooling—A review. *Solid-State Electronics* **15**, 1121-1140 (1972).

16. Son, J. S. *et al.* All-inorganic nanocrystals as a glue for BiSbTe grains: design of interfaces in mesostructured thermoelectric materials. *Angew. Chem. Int. Ed.* **53**, 7466-7470 (2014).

17. Hu, L. P. *et al.* Shifting up the optimum figure of merit of p-type bismuth telluride-based thermoelectric materials for power generation by suppressing intrinsic conduction. *NPG Asia Materials* **6**, e88 (2014).

18. Zhao, X. B. *et al.* Bismuth telluride nanotubes and the effects on the thermoelectric properties of nanotube-containing nanocomposites. *Appl. Phys. Lett.* **86**, 062111 (2005).

19. Liu, W.-S. *et al.* Thermoelectric Property Studies on Cu-Doped n-type $Cu_xBi_2Te_{2.7}Se_{0.3}$ Nanocomposites. *Adv. Energy Mater.* **1**, 577-587 (2011).

20. Hu, L. *et al.* Tuning Multiscale Microstructures to Enhance Thermoelectric Performance of n-Type Bismuth-Telluride-Based Solid Solutions. *Adv. Energy Mater.* **5**, 1500411 (2015).

21. Min, Y. *et al.* Surfactant-free scalable synthesis of Bi_2Te_3 and Bi_2Se_3 nanoflakes and enhanced thermoelectric properties of their nanocomposites. *Adv. Mater.* **25**, 1425-1429 (2013).

22. Scheele, M. *et al.* ZT enhancement in solution-grown $Sb_{(2-x)}Bi_xTe_3$ nanoplatelets. *ACS Nano* **4**, 4283-4291 (2010).

23. Dong, G. H., Zhu, Y. J. & Chen, L. D. Microwave-assisted rapid synthesis of Sb_2Te_3 nanosheets and thermoelectric properties of bulk samples prepared by spark plasma sintering. *J. Mater. Chem.* **20**, 1976 (2010).

24. Mehta, R. J. *et al.* Seebeck and figure of merit enhancement in nanostructured antimony telluride by antisite defect suppression through sulfur doping. *Nano Lett.* **12**, 4523-4529 (2012).

25. Soni, A. *et al.* Interface driven energy filtering of thermoelectric power in spark plasma sintered $Bi_2Te_{2.7}Se_{0.3}$ nanoplatelet composites. *Nano Lett.* **12**, 4305-4310 (2012).

26. Soni, A. *et al.* Enhanced thermoelectric properties of solution grown $Bi_2Te_{3-x}Se_x$ nanoplatelet composites. *Nano Lett.* **12**, 1203-1209 (2012).

27. Zhang, G. *et al.* Rational synthesis of ultrathin n-type Bi_2Te_3 nanowires with enhanced thermoelectric properties. *Nano Lett.* **12**, 56-60 (2012).

28. Zhang, C. *et al.* Controlled growth of bismuth antimony telluride $Bi_xSb_{2-x}Te_3$ nanoplatelets and their bulk thermoelectric nanocomposites. *Nano Energy* **15**, 688-696 (2015).

29. Scheele, M. *et al.* Synthesis and Thermoelectric Characterization of Bi_2Te_3 Nanoparticles. *Adv. Funct. Mater.* **19**, 3476-3483 (2009).

30. Sun, S. *et al.* Template-free solvothermal synthesis and enhanced thermoelectric performance of Sb_2Te_3 nanosheets. *Journal of Alloys and Compounds* **558**, 6-10 (2013).

31. Kim, C., Kim, D. H., Kim, J. T., Han, Y. S. & Kim, H. Investigation of reaction mechanisms of bismuth tellurium selenide nanomaterials for simple reaction manipulation causing effective adjustment of thermoelectric properties. *ACS Appl. Mater. Interfaces* **6**, 778-785 (2014).

32. Fu, J. *et al.* Bi_2Te_3 nanoplates and nanoflowers: Synthesized by hydrothermal process and their enhanced thermoelectric properties. *CrystEngComm* **14**, 2159 (2012).

33. Lu, Z. *et al.* Aqueous solution synthesis of (Sb, Bi)$_2$(Te, Se)$_3$ nanocrystals with controllable composition and morphology. *J. Mater. Chem. C* **1**, 6271 (2013).

34. Son, J. S. *et al.* n-Type nanostructured thermoelectric materials prepared from chemically synthesized ultrathin Bi$_2$Te$_3$ nanoplates. *Nano Lett.* **12**, 640-647 (2012).

35. Dirmyer, M. R., Martin, J., Nolas, G. S., Sen, A. & Badding, J. V. Thermal and electrical conductivity of size-tuned bismuth telluride nanoparticles. *Small* **5**, 933-937 (2009).

36. Zhang, J. *et al.* Raman spectroscopy of few-quintuple layer topological insulator Bi$_2$Se$_3$ nanoplatelets. *Nano Lett.* **11**, 2407-2414 (2011).

37. Kim, H. S., Gibbs, Z. M., Tang, Y., Wang, H. & Snyder, G. J. Characterization of Lorenz number with Seebeck coefficient measurement. *APL Mater.* **3**, 041506 (2015).

38. Klemens, P. G. Thermal Conductivity and Lattice Vibrational Modes. *Solid State Physics* **7**, 1-98 (1958).

39. Puneet, P. *et al.* Preferential scattering by interfacial charged defects for enhanced thermoelectric performance in few-layered n-type Bi$_2$Te$_3$. Sci. Rep. 3, 3212 (2013).

40. German, R. M., Suri, P. & Park, S. J. Review: liquid phase sintering. J. Mater. Sci. 44, 1-39 (2008).

Acknowledgements

Author contributions

C. Z. and Q. X. conceived and designed the experiments. Q.X. directed the experiments. C. Z. carried out the experiments of solution-growth and devices fabrications, SEM, XRD and thermoelectric transport measurements and analysed those data. F.J.B., M.d.l.M. and J.A. made the TEM samples and conducted the TEM-related characterizations and analysis. C. Z., Z.L. and K.A.K. carried out the SPS experiments for bulk pellets. D.P. contributed to helpful discussions on transport properties. Z.F.R. measured the thermoelectric properties as elevated temperatures. C. Z. and Q.X. wrote the manuscript. All the authors commented on the manuscript.

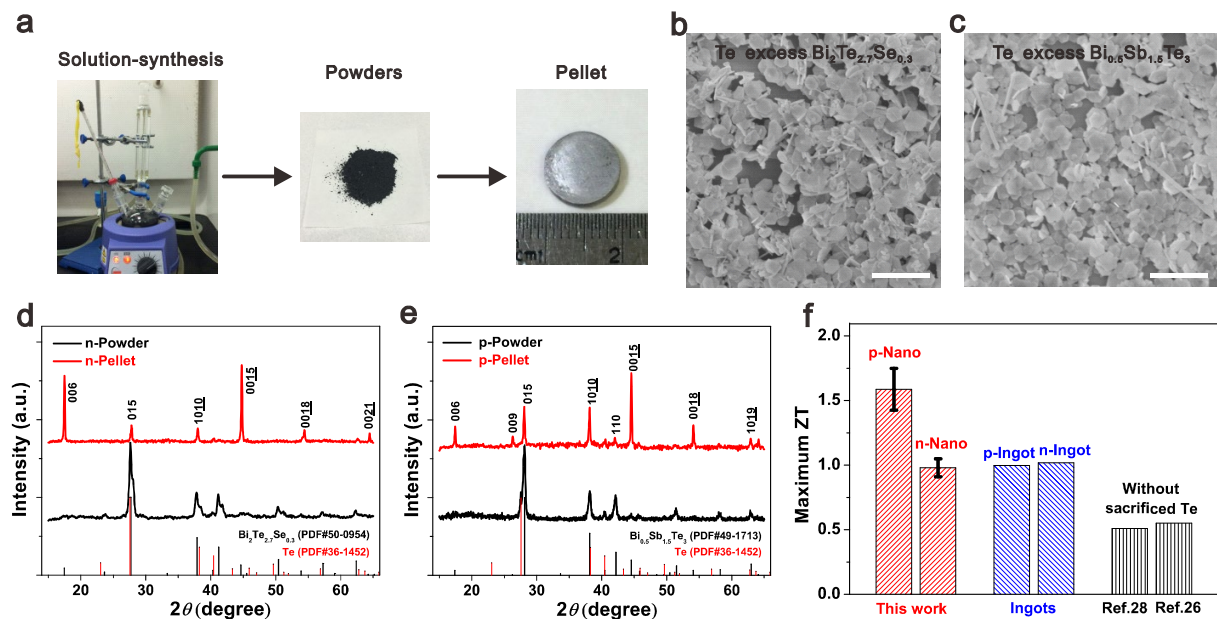**Additional Information**

Figures and Legends

Figure 1. Bottom-up approach for high-performance thermoelectric materials. (a) Schematic representation of the bottom-up approach to nanostructured bulk pellet in two steps: solution-synthesis to get powders and spark plasma sintering process to achieve bulk pellets. **(b)(c)** Scanning electron micrographs of Te-$Bi_2Te_{2.7}Se_{0.3}$ and Te-$Bi_{0.5}Sb_{1.5}Te_3$ mixtures respectively, revealing the nanowires and nanoplates morphology in the powders. Scale bars, 2 μm. **(d)(e)** X-ray diffraction patterns of powders and pellets of the n-Nano and p-Nano samples respectively, showing the distinct Te phase in the powders but undetectable in pellets. **(f)** The maximum figure of merit ZT of our nanobulk samples in this work (n-type and p-type nanobulks), commercial ingots (n-type and p-type ingots) and nanobulk samples without sacrified Te (p-type in Ref.28 and n-type in Ref.26) in the testing temperature range 5-370 K.
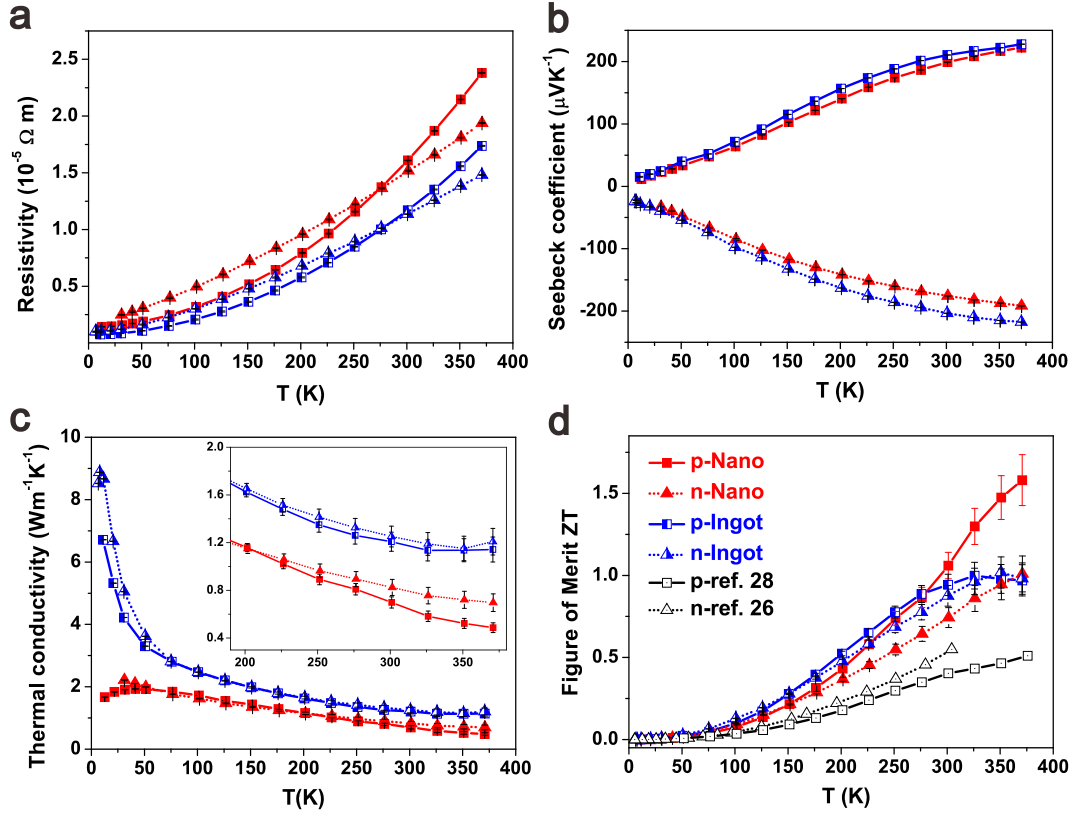
Figure 2. Thermoelectric properties of our nanobulk samples (n-type n-Nano and p-type p-Nano) and commercial ingots (n-type n-Ingot and p-type p-Ingot). (a) Temperature dependence of electrical resistivity. **(b)** Temperature dependence of Seebeck coefficient. **(c)** Temperature dependence of thermal conductivity. The inset corresponds to the enlarge region of (c) in the range 200-370 K. **(d)** Temperature dependence of the figure of merit ZT. The plots of p-ref.28 and n-ref. 26 are the p-type and n-type nanobulk samples in our previous work respectively, which are prepared by the similar bottom-up approach but without excess Te as sacrificial additive. All the figures share the same annotation as shown in (d). The error bars are the deviations of measurements in each test point.
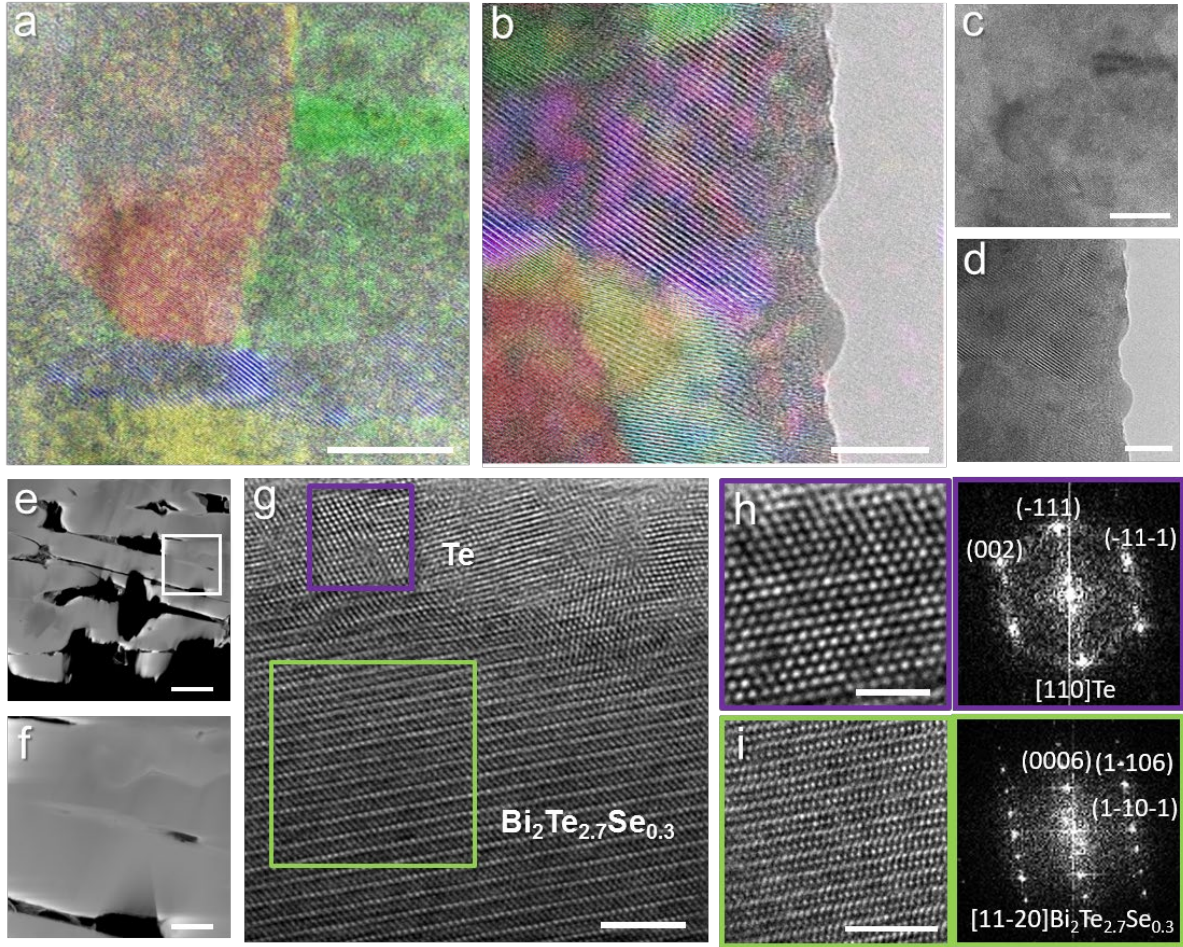
Figure 3. TEM characterizations of the n-Nano bulk samples. (a)(b) HRTEM combined with phase filtered coloured images of n-Nano bulk samples in planar view, revealing various nanograins with different orientations. Scale bars, (a) 20 nm and (b) 10 nm. **(c)(d)** The corresponding original HRTEM images of (a)(b), respectively. Scale bars, (c) 20 nm and (d) 10 nm. **(e)** Cross-section low magnification HAADF STEM image of n-Nano. Cracks are found in grain boundaries during the thinning process of TEM samples. Scale bar, 2 μm. **(f)** Magnified detail of the white framed area in (e). Scale bar, 0.5 μm. **(g)** Cross-section HRTEM image of the n-Nano sample near a grain boundary, showing the existence of segregated Te phase at the grain boundary. Scale bar, 5 nm. **(h)(i)** Zooming HRTEM details of crystallographic phase of Te and $Bi_2Te_{2.7}Se_{0.3}$ respectively in the framed areas of (g), along with their corresponding indexed power spectra. Scale bars, (h) 2 nm and (i) 5 nm.
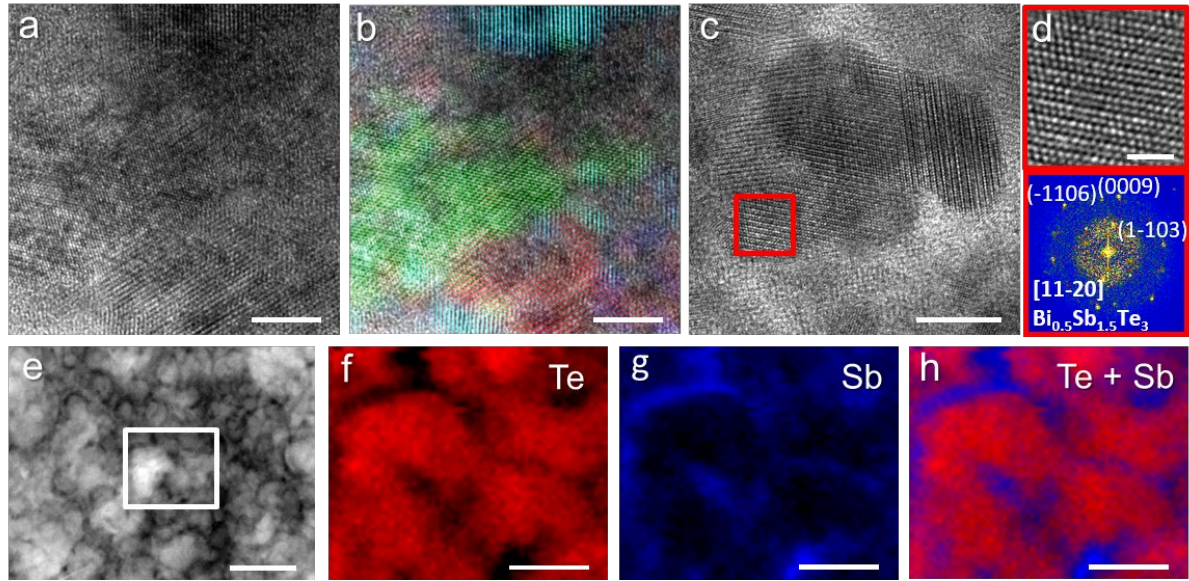
Figure 4. TEM analysis of the p-Nano bulk samples. (a)(b) HRTEM combined with phase filtered coloured images of the p-Nano bulk sample, showing nanograins with different orientations. Scale bars, 5 nm. **(c)** HRTEM image of the p-Nano in another region. Scale bar, 10 nm. **(d)** Enlarged HRTEM details of the crystallographic phase of $Bi_{0.5}Sb_{1.5}Te_3$ in the red framed area of (c), along with the corresponding indexed power spectrum. Scale bar, 2 nm. **(e)** Low magnification HAADF image of the p-Nano sample. Scale bar, 50 nm. **(f)(g)** The EELS elemental mapping of extracted Te and Sb signals, respectively, in the white framed region of (e). Scale bars, 20 nm. **(h)** Overlay of the extracted Te and Sb elemental maps, showing Sb-enriched regions in some boundary areas. Scale bar, 20 nm.
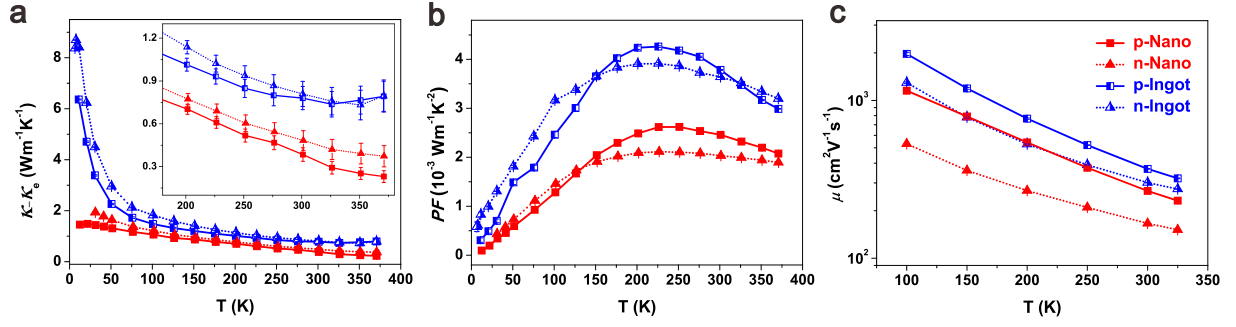
Figure 5. Comparison of the calculated lattice thermal conductivity, power factor and charge-carrier mobility. (a) Temperature dependence of lattice thermal conductivity (κ_l), which are calculated by subtracting the electronic thermal conductivity ($\kappa_e = LT/\rho$) from the total thermal conductivity. The inset corresponds to the enlarge region of (a) in the range 200-370 K. **(b)** Temperature dependence of power factor PF (S^2/ρ). The calculated κ_l and PF are basing on the measurements shown in Figure 2. **(c)** Temperature dependence of charge-carrier mobility μ calculated by the formula $\mu = 1/(n\rho e)$, where the charge density n are determined by the Hall measurements and the electrical resistivity ρ is from the data in Figure 2a. All the figures share the same annotation as shown in (c), which are the same as Figure 2.